Research paper

Glycine-assisted hydrothermal synthesis of pure and europium doped CeO_2 nanoparticles and their structural, optical, photoluminescence, photocatalytic and antibacterial properties

S. Gnanam [a,*], J. Gajendiran [b,*], J. Ramana Ramya [c], K. Ramachandran [d], S. Gokul Raj [e]

[a] *Department of Physics, School of Basic Sciences, Vels Institute of Science, Technology & Advanced Studies (VISTAS), Pallavaram, Chennai-600 117, Tamilnadu, India*
[b] *Department of Physics, Vel Tech Rangarajan Dr. Sagunthala R&D Institute of Science and Technology, Avadi, Chennai 600 062, India*
[c] *National Center for Nanoscience and Nanotechnology, University of Madras, Chennai-600025, India*
[d] *Department of Physics, SRMIST, Vadapalani Campus, Chennai-600026, India*
[e] *Department of Physics, C. Kandaswami Naidu College for Men, Annanagar, Chennai-600102, Tamilnadu, India*

ARTICLE INFO

ABSTRACT

Pure and europium doped cerium dioxide (CeO_2) nanoparticles were synthesized for the first time via glycine-assisted hydrothermal process and comparatively investigated their structural, optical, photoluminescence, photocatalytic and antibacterial properties. The synthesized pure cerium dioxide (PCDO) and Eu^{3+} doped cerium dioxide (ECDO) samples were subjected to the powder XRD, W-H plot, TEM, EDX, XPS, UV–visible, PL, photocatalytic and antibacterial studies. Based on the above analysis, ECDO found relatively smaller size, higher band gap and oxygen vacancy defects, better photocatalytic degradation and antibacterial properties compared to the PCDO sample. Moreover, the ferromagnetism characteristics of the ECDO were found in the M−H loop.

1. Introduction

In recent years, Rare Earth Elements (REE) has been incorporated into semiconductor metal oxides to increase the efficiency of luminescence through the process of energy conversion. The optical characteristics of rare earth ions trapped in host lattices have provided a great deal of fundamental and technological points of view. cerium dioxide (CeO_2) nanomaterials are some of the active versatile rare earth metal oxide nanomaterials in the lanthanide series, that are widely used in catalysts, oxygen sensors, ultraviolet blocking materials, luminescence and solid oxide fuel cells due to their unique cubic fluorite structure and physical and chemical properties. Numerous researchers have focused on the synthesis of doped CeO_2 nanomaterials by using high energy ball milling [1], solid state reaction [2–4], combustion [5–9], sol–gel [10,11], electrochemical deposition [12], Pulsed laser deposition [13], electrospun [14], Spray pyrolysis [15–19], microwave reflux [20–22], thermal evaporation [23], precipitation [24–29], and hydrothermal/ solvothermal method [30–38] for optical and magnetic studies. The strong nodal optical absorption edge in the ultraviolet portion and high nodal emission peaks in the visible portion, moderate optical band gap and ferromagnetic activity of nanostructured doped CeO_2 samples are

found in the optical absorption spectra, RTPL and magnetic hysteresis studies. The above properties can be used in the applications of electronics and spintronic devices.

In this current work, we used a lower reaction temperature via the glycine-assisted hydrothermal route to obtain 10–13 nm of ECDO and PCDO nanoparticles with good dispersed particles. For the first time, the structural, surface particle shape, optical, photoluminescent, photocatalytic, antibacterial and magnetic activity of ECDO nanoparticles have been reported using the glycine-assisted hydrothermal process. The interplay in the trivalent metal ion europium (Eu^{3+}) dopant in the CeO_2 sample represents an increased band gap, oxygen vacancy defects, reduced particle size, and improved photocatalytic degradation, antibacterial relative to the pure CeO_2 sample in the UV–visible, PL, photocatalytic and antibacterial studies.

2. Experimental procedure

2.1. Synthesis of pure and Eu-doped CeO_2 nanoparticles

0.130 g of cerium (III) nitrate hexahydrate ($Ce(NO_3)_3 \cdot 6H_2O$) was dissolved in aqueous solvent and 0.024 g of sodium hydroxide pellets
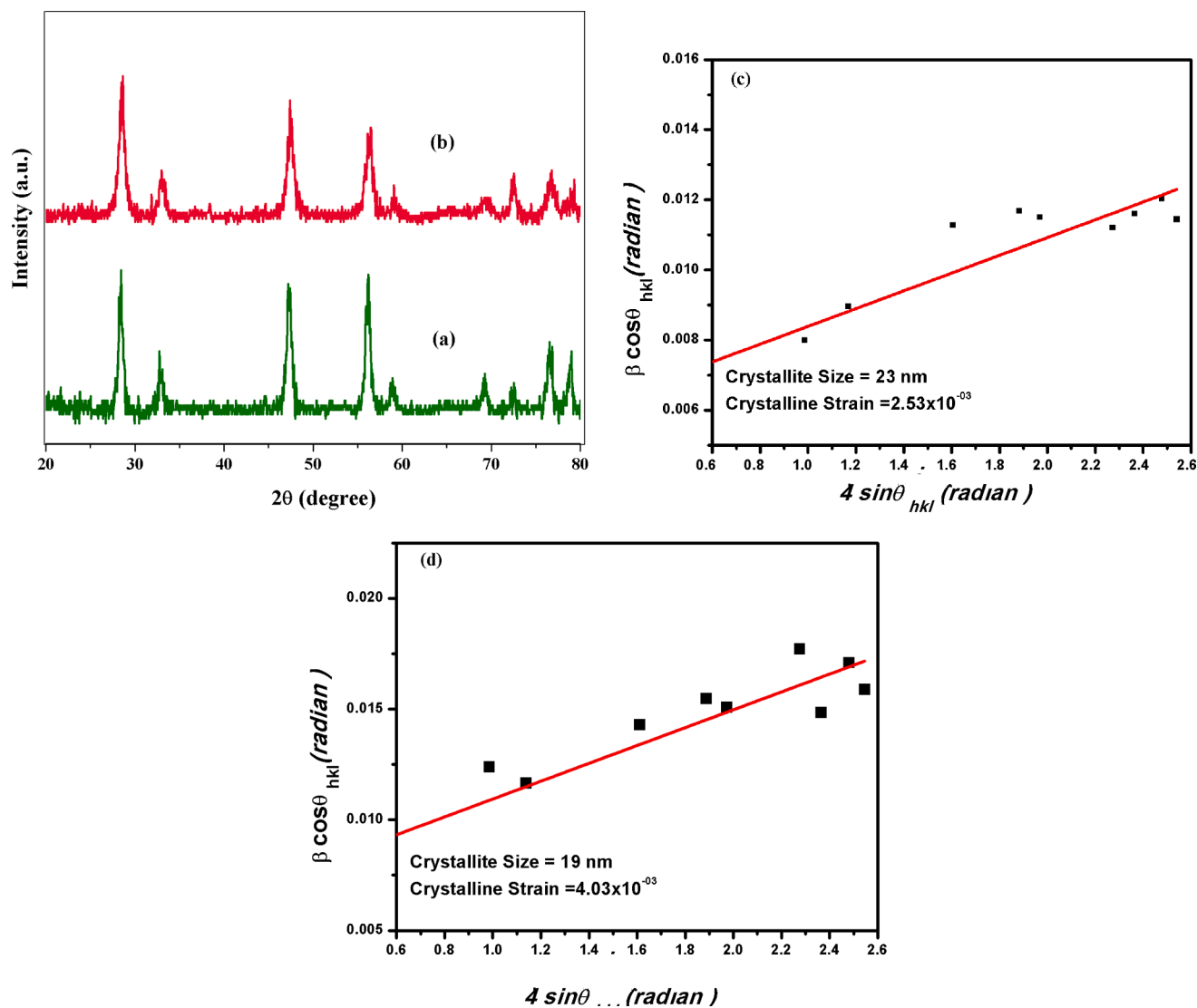

Fig. 1. (a-b) Powder XRD pattern and (c-d) W-H plot of PCDO and ECDO samples.

were dissolved in a separate beaker solution. Subsequently, 3 mol % of europium (III) nitrate hexahydrate (Eu(NO$_3$)$_3$·6H$_2$O) was combined with the cerium nitrate transparent solution. Then 0.022 g of amino acid (glycine) was added to the solution mentioned above. A drop-wise addition of sodium hydroxide solution to the above mixture was followed by the development of colloidal-solutions. This mixture was transferred to the 100 mL capacity Teflon-lined stainless steel autoclave for a 10 hrs reaction at 150 °C and the products were collected and washed several times with ethanol. Finally, in order to obtain the Eu doped CeO$_2$ (ECDO) samples, the intermediate products were calcined at 400 °C for 2hrs. The same procedure was followed for the preparation of the pure CeO$_2$ (PCDO) sample without the addition of the doping material to the precursor solution.

2.2. Characterization

Powder XRD patterns of PCDO and ECDO materials were registered at a scattering angle in the range of 20-80° using the Schimadzu model: XRD 6000 powder X-ray diffractometer instrument applying CuK$_\alpha$ (λ = 0.154 nm) radiation. The burned PCDO and ECDO ceramics powder was analyzed on the H-800 TEM (Hitachi, Japan) TEM instrument by applying acceleration voltage of 10^5 V, accompanied by an EDX analysis attachment for the elemental analysis. Ultraviolet–visible absorption

spectra of PCDO and ECDO samples were taken using the Varian Cary 5E spectrophotometer. The PL emission spectra of the PCDO and ECDO materials were tested using the Perkin-Elmer lambda 900 spectropho-tometer with the Xenon (Xe) inert gas as a light source. The room temperature magnetic characteristics of the ECDO sample are examined on the EG&G PARC VSM 155 model.

3. Results and discussion

The structural characteristics of the synthesized PCDO and ECDO ceramic samples were studied using the powder X-ray diffraction (XRD) analysis. All the scattering peaks corresponding to their planes were indexed in the XRD pattern for both the samples, as displayed in Fig. 1 (a-b). The position of the scatter angles and their respective planes in the XRD pattern were perfectly consistent with the reported values of the standard scatter peak position of cerium dioxide (JCPDS number 81–0792), which indicated that the prepared samples confirmed the formation of the cubic fluorite crystalline phase [6]. Further, no additional scattering peaks were found in the XRD pattern of the ECDO sample, suggesting that the crystalline phase did not alter when the dopant was added to the host lattice. Due to the incorporation of euro-pium in the cerium dioxide lattice, the europium (Eu^{+3}) ionic radius (0.095 nm) is significantly lower than that of the ionic radius of cerium
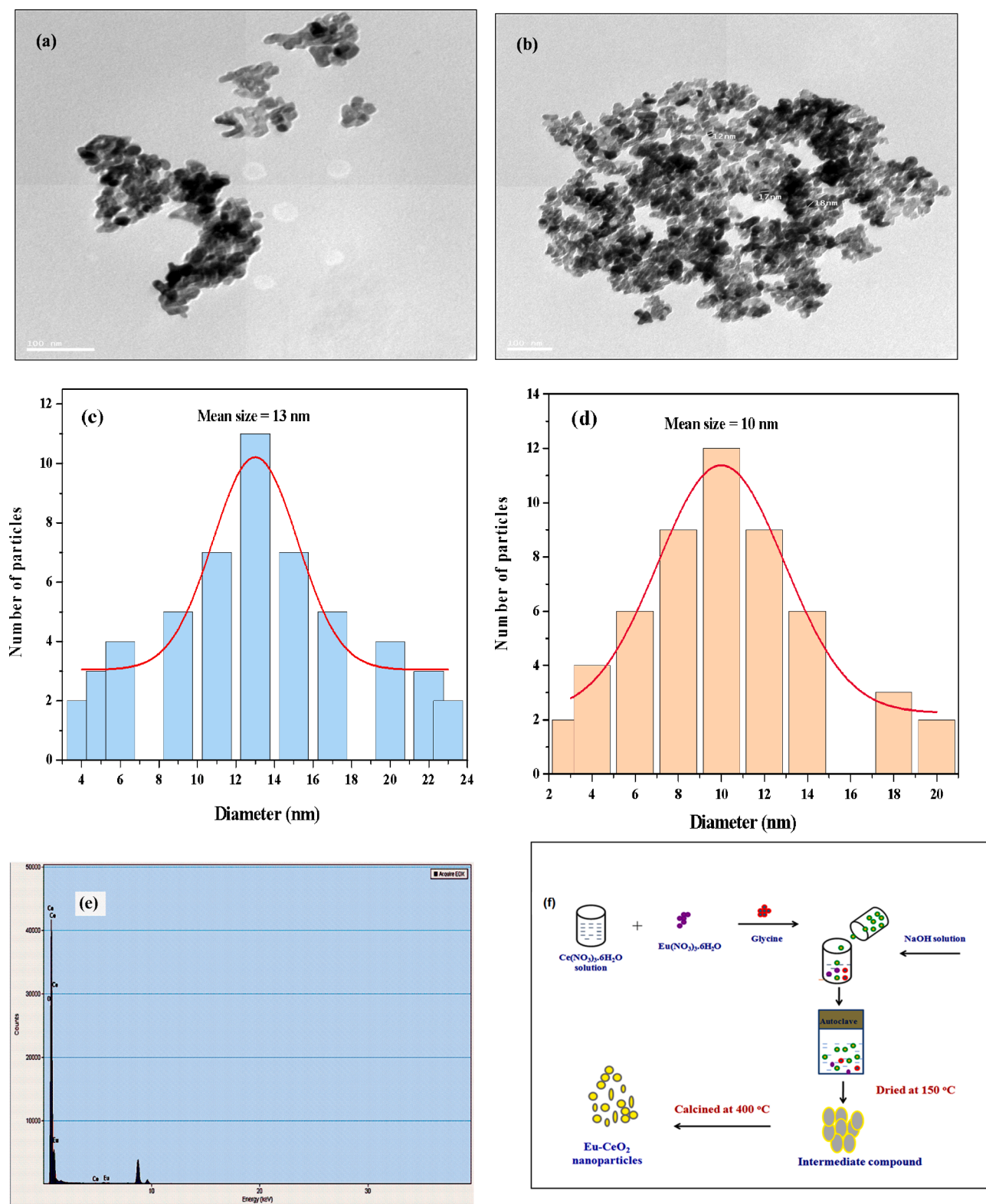
Fig. 2. TEM images of (a) PCDO and (b) ECDO samples, Statistical histogram of particle size distribution images of the (c) PCDO and (d) ECDO samples (e) EDX spectrum of ECDO sample and (f) Schematic formation of ECDO sample.

(Ce^{4+}) (0.097 nm) [39]. In addition, significant broadening of the scattering peaks was observed in the ECDO sample compared to the PCDO sample. The mean crystallize sizes of the ECDO and PCDO samples were calculated using Scherrer's equation [5], as 10 and 13 nm, respectively.

The lattice strains of PCDO and ECDO (Williamson-Hall (W-H) plot) are also displayed in Fig. 1 (c-d). The ECDO sample was found to have linear fit slopes higher than the PCDO sample in the plot, resulting in the presence of high strain in the ECDO sample. Using the scattering plane (1 1 1) (Table 1), the lattice constant (a) values of PCDO and ECDO

Table 1

Scattering angles (2θ) and their respective planes, Full Width Half Maximum (FWHM), d-spacing and crystallite size of the PCDO and ECDO samples.
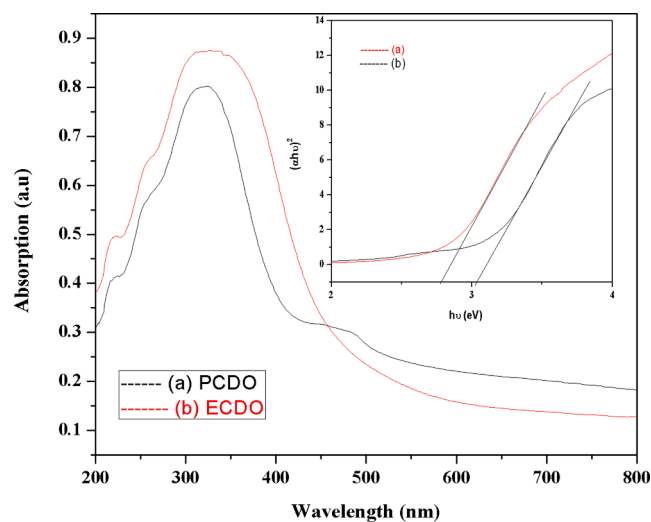
Planes	PCDO sample				ECDO sample			
	2θ	FWHM (Radian)	d-spacing (Å)	Crystallite size from Scherrer's equation (nm)	2θ	FWHM (Radian)	d-spacing (Å)	Crystallite size from Scherrer's equation (nm)
(1 1 1)	28.40°	0.76	3.14	12.0	28.52°	0.93	3.13	9.8
(2 0 0)	32.91°	0.69	2.75	13.4	33.04°	0.91	2.71	10.2
(2 2 0)	47.30°	0.79	1.90	12.3	47.46°	1.00	1.88	9.7
(3 1 1)	56.16°	0.75	2.40	13.4	56.29°	1.10	1.63	10.1
(2 2 2)	58.91°	0.80	1.57	12.5	59.08°	1.13	1.57	9.0
(4 0 0)	69.22°	0.74	1.35	14.5	69.33°	1.39	1.32	7.9

Table 2

Mean crystallite size, crystalline strain (ε), intercept and slope values of PCDO and ECDO samples.

Samples	Average crystallite size (D; nm)		Lattice strain from W-H plot $\varepsilon = \beta\cos\theta \times D/(0.9\lambda \times 4\sin\theta)$	Intercept	Slope
	From Scherrer $D = 0.89\lambda/\beta\cos\theta$	From the W-H plot $D = 0.9\lambda/\beta\cos\theta \times 4\varepsilon\sin\theta$			
PCDO	20	23	2.53×10^{-3}	0.00586	0.00253
ECDO	15	19	4.03×10^{-3}	0.00691	0.00403

samples are calculated as 5.43 and 5.42 Å by the lattice constant equation a = $d_{hkl}/\sqrt{(h^2 + k^2 + l^2)}$. Thus, the volumes of the PCDO and ECDO unit cells are determined as 160.10 and 158.34 ($Å^3$) using the lattice constant values. The lattice constant and the volume of the PCDO and ECDO samples obtained values closely matched with the reported values of the transition metal doped (Cu, Zn, Cr) CeO_2 materials [6]. In the ECDO sample, the lattice constant and the volume were relatively decreasing compared to the PCDO sample. In addition, we noted that the scattering angles value of the ECDO sample was slightly shifted to a higher position compared to that of the PCDO in Table 1, was detected in the XRD patterns. The reason for the shift in the higher angle of the ECDO sample in the XRD is due to the smaller crystallite size. From Table 2, it can be noted that the PCDO and ECDO crystallite size values are calculated using the Debye Scherer's formula, which is fairly comparable with the W-H formula. Table 2 shows that the crystalline strain value of the ECDO sample is relatively lower compared to that of the PCDO sample. It is also noted that the intercept and slope value of the ECDO sample is relatively lower than that of the PCDO sample from the W-H data.

The synthesized PCDO and ECDO samples were examined in the Transmission Electron Microscopy (TEM) analysis to measure their grain size. The grain size of the PCDO and ECDO materials was measured as 13 and 10 nm, respectively (Fig. 2(a-b)), consistent with the estimated crystallite size using Scherrer's formula. In addition, based on the above TEM result, it could be inferred that the doping additive in the precursor controls the crystalline growth and reduces the grain size. The lattice interplanar distances were measured to be 0.31 nm for the ECDO sample in the HR-TEM image (Fig.S1) as depicted in the Supporting Information. The particle size distribution histogram statistics are shown in Fig. 2 (c-d). The majority of the particle size frequencies were observed in the TEM picture to be 10 and 13 nm for PCDO and ECDO samples, respectively. The prepared ECDO sample was tested on the Energy Dispersive X-ray (EDX) spectrum attached to the TEM for the identification of the elements as shown in Fig. 2e, which confirms the presence of elements such as Ce, O and Eu. It clearly showed the incorporation of cerium oxide by the Eu metal ion dopant. The synthesized ECDO sample was performed on the X-ray photoelectron spectrum (XPS, model- PHI 5000Versa Probe III instrument) (Fig.S2) and its plot between the binding energy (eV) and count/second was shown in the Supporting Information. It provides information about the binding energy of

Fig. 3. UV–visible absorption spectra of (a) PCDO and (b) ECDO samples. The inset shows Tauc plot of (a) PCDO and (b) ECDO samples.

chemical elements and the oxidation states found in the synthesized samples. For the ECDO sample from the XPS analysis, Ce, O and Eu were observed, which indicates that the Eu element is incorporated in the cerium oxide material for the synthesized doped sample. The findings of the above XPS further reconfirm the results of the EDX. The FT-IR spectra of the PCDO and ECDO dried samples results are given in the Supporting Information (Fig.S3). We could confirm that the PCDO and ECDO dried samples are glycine-coated on the surface of cerium oxide material in the FT-IR spectra.

The formation mechanism of the glycine-assisted hydrothermal synthesis of ECDO nanoparticles is shown in Fig. 2f. In this work, attempts have been made to use amino acids such as glycine-assisted in the hydrothermal process instead of in the surfactants-assisted process. In particular, the synthesis of PCDO and ECDO nanoparticles using glycine helps to achieve the required size and shape. It is well-known that amino acids have the inherent properties of directing and assembling superstructures. In this case, glycine tends to serve as a capping agent and its presence in the cerium hydroxide colloidal solution serves to obtain a controlled grain size of the cerium dioxide synthesized sample. The concentration of glycine decreased after mineral formation, suggesting the removal of amino acids from the solution through interaction with the cerium hydroxide minerals. In addition, the glycine-coated cerium di oxide was beneficial as it prevented the agglomeration of the particles. As a consequence, aggregates in clusters have also been found to increase. Each individual aggregate consisted of a mixture of several superfine particles with sizes of less than 15 nm. In this case, glycine produces a favorable site for the growth of particulate assemblies. Furthermore, the trivalent metal ion doping (Eu^{3+}) also alters the particle size of cerium oxide, which is in good agreement with the results of XRD and TEM.

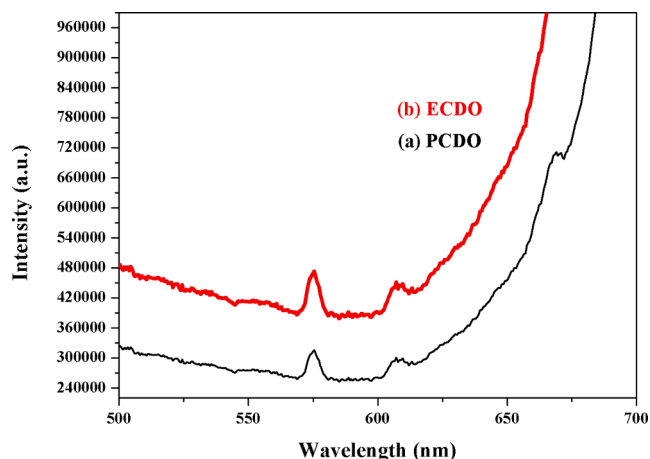Relatively high optical absorption and shifts to higher frequency (ie

Fig. 4. (a-b) RT-PL spectra of PCDO and ECDO samples.

Fig. 5. M−H loop of ECDO nanoparticles.

absorption shifts to shorter wavelength) for the ECDO sample compared to the PCDO can be clearly detected in the UV–visible absorption spectra (Fig. 3(a-b)). This was due to the smaller crystalline size of the ECDO sample. When light radiation occurs on a smaller crystallite size of ECDO material, relatively large numbers of active sites contribute to light radiation and are reflected to produce relatively high absorption of light. A strong increase in absorption appears at ~ 326 nm caused by the excitons and the electrons' transition, which takes place between the valence and conduction band of cerium dioxide [26,40]. This strong absorption portion indicated that the electron hopped from the 2P valence band of O^{2-} to the 4f band of Ce^{4+} [5]. The optical band gap values for the PCDO and ECDO nanoparticles are determined as 2.73 and 3.03 eV, respectively, with the help of the $h\nu$ vs $(\alpha h\nu)^2$ (Tauc plots) as displayed inset of Fig. 3 (a-b).

The PCDO and ECDO emission behavior can be analyzed using room temperature- Photoluminescence (RT-PL) spectra. Broad nodal visible emission peaks for both PCDO and ECDO samples were detected in the PL spectra as shown in Fig. 4 (a-b). It showed the emission band in the visible portion characteristic of the shallow traps present in the PCDO and ECDO materials. Relatively an intense emission peak of 575 and 607 nm was detected for the ECDO sample due to the highly strained and distorted environment around the Eu^{3+} ions in the cerium dioxide lattice compared to the PCDO sample, which is in good agreement with the obtained crystalline strain values from the W-H plot results. An intense PL emission peaks for ECDO sample were observed compared to the PCDO sample due to the higher oxygen vacancy defects [41,42]. It was also due to the relatively small crystallite ECDO sample, which represents a large number of sites in the crystal lattice when interacting with the light source. Anandan et al. [41] and Liqiang et al. [42] have reported that the higher oxygen vacancy defects and the semiconductor
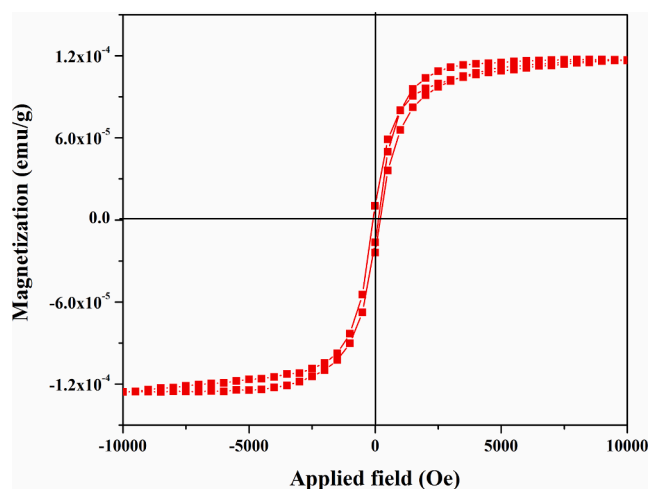
nanomaterial's surface area play a vital role in improving the photodegradation activity. The ECDO sample is believed to have a strong visible emission band (~575 and 607 nm) due to Eu^{3+} transitions [39]. Furthermore, there is slight shift in the position of the emission peaks observed in PCDO and ECDO samples.

Table 3 shows that the present ECDO is comparable or better than the previous reported nanostructured materials. On the basis of the above literatures, it can be found that there are certain limitations in obtaining ECDO nanostructures such as larger particle sizes, higher calcined temperatures and special conditions. In our current work, ECDO nanoparticles with a particle size of 15 nm are prepared without any special condition or higher calcined temperature.

Fig. 5 displays the M−H loop of the nanostructured ECDO sample. A small loop of hysteresis was observed, indicating that the room temperature's ferromagnetic (RTFM) activity had a slight magnetic effect. This was due to the lesser interaction between the Eu dopant and the CeO_2 host when the force of the magnetic lines was applied to the positive and negative direction of the x-axis. The calculated values of coercive force and magnetic saturation of the ECDO sample are 100 Oe and 1.149×10^{-4} emu/g. In addition, the magnetic susceptibility (χ) and relative permeability (μ_r) values of ECDO are calculated as 1.149 and 2.28, respectively. The nanostructured ECDO is therefore confirmed as ferromagnetic material for the obtained values of χ and μ_r. Niruban Bharathi et al. [6] reported the RT-FM in pure and doped nanostructured CeO_2 samples and revealed the origin of the ferromagnetic properties as the reciprocating interaction between the electron spin moments, as a consequence of which the oxygen vacancies present on the surface of the CeO_2 nanoparticles were formed. In general, the weak ferromagnetic behavior of transition metal and rare earth metal doped CeO_2 material

Table 3
Comparative study of the preparation method, calcined temperature, morphology, particle size, PL emission bands and optical band gap in our work and previous reports of Eu doped CeO_2 nanostructures.

| S. No	Preparation method	Calcined temperature	Morphology	Particle size (nm)	PL emission bands (nm)	Optical band gap (eV)	Ref
1	Electrospun	500–900 °C	Nanotubes	500	590,609	–	Fang et al. [14]
2	Spray pyrolysis	900–1100 °C	Plate	50–200	592,612,632,714	2.29–3.28	Jung et al. [15]
3	Spin on pyrolysis	400–700 °C	Thin film	110	591,610,624	–	Fujihara et al. [16]
4	Sol-gel	600 °C	Spherical	22–46	590,610,630, 650	–	Yildirim et al. [18]
5	Hydrothermal	500–1000 °C	Spherical	11–33	580,591,610,632,638,655,682,696	2.07–2.98	Choudhary et al. [31]
6	Green combustion	600 °C	Flake	20–25	540–580,593,613, 625–640,708	–	Malleshappa et al. [39]
7	Thermolysis	500 °C	Spherical	5–55	596,636,654	–	Silva et al. [43]
8	Hydrothermal	400–800 °C	Rod	Length > 100	592, 620	–	Gao et al. [44]
9	Micro emulsion	500–1000 °C	–	–	591,611,632	–	Parvilescu et al. [45]
10	Hydrothermal	400 °C	Spherical	15–20	575, 607	3–23-3.24	Present work
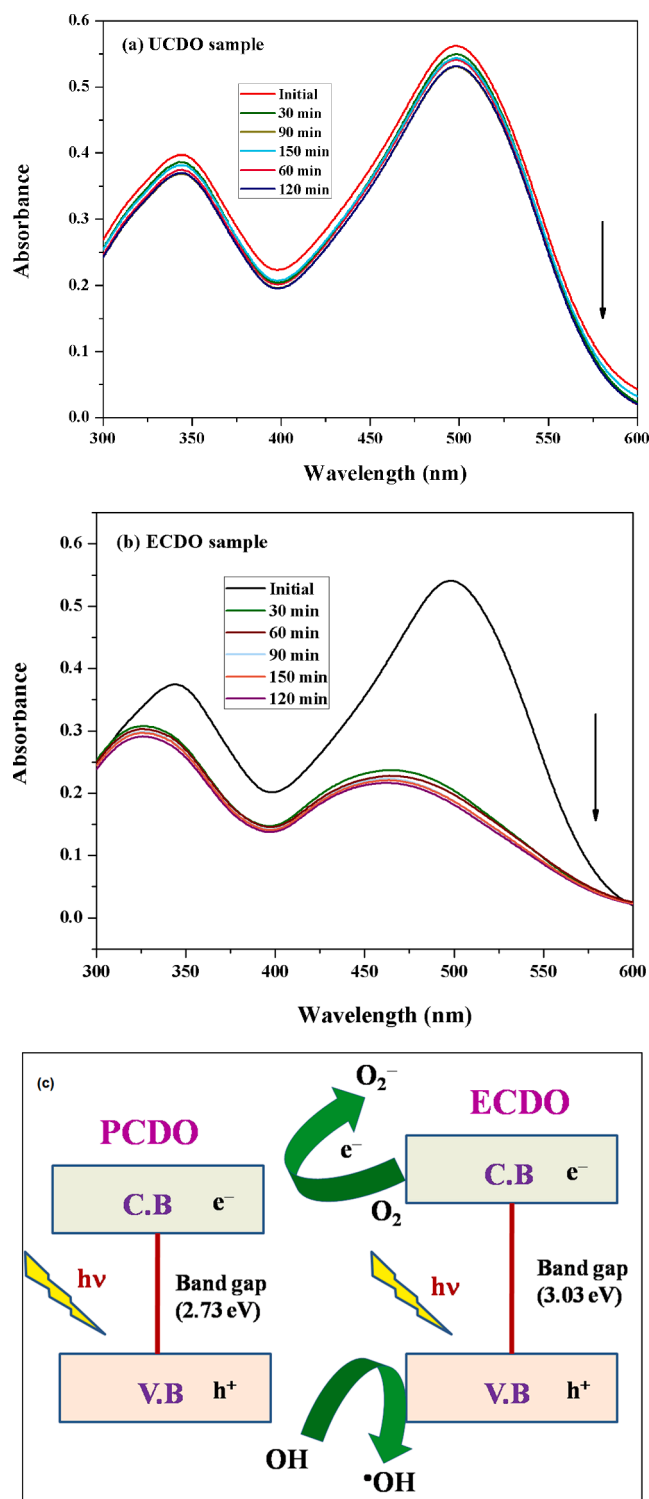
Fig. 6. UV–visible spectra of the photodegradation of CR dye/synthesized samples (a) PCDO, (b) ECDO and (c) Schematic formation of photodegradation of CR dye/synthesized PCDO and ECDO samples.

has been found in the M−H loop [26–29], which may be suitable for spintronics- based device applications.

The Supporting Information includes the photocatalytic experimental details of the PCDO and ECDO samples as a photocatalyst using the Congo red dye. UV–visible spectra were taken at different time intervals from the PCDO and ECDO samples/congo red dye solution, as shown in Fig. 6 (a-b). We could see that with the increasing light

irradiation time, which reveals the degradation of dye molecules, the optical absorption peak intensity decreased noticeably. The photodegradation efficiency of the PCDO and ECDO samples was determined to be 14% and 67% for the PCDO and ECDO samples using this equation (η = 1-C/C_0 × 100, where, η- photodegradation efficiency, C_0 and C represent the before and after photodegradation of organic dye molecule). Due to the high oxygen vacancy defects and high surface area, better photodegradation was obtained for the ECDO sample compared to the PCDO [41,42]. The schematic reaction of photodegradation of synthesized PCDO and ECDO material as shown in Fig. 6c.

The described photocatalytic degradation process is given below. When the light irradiated continuously on the ECDO material, Eu dopant was jumped to the excited state, the excited electrons of Eu accumulated to the conduction band (C.B) of the CeO_2. The C.B electrons then searched and trapped the surface adsorbed oxygen to create the $O_2^{-\bullet}$ radical that would further react with the surface adsorbed water molecules to produce the hydroxide radical $OH^\bullet$. The photoinduced $OH^\bullet$ radicals can degrade the organic pollutants to put an end product carbon dioxide and water.

The antibacterial behaviour of the PCDO and ECDO samples were examined against E. Coli (gram-negative strain) and S. aureus (gram-positive strain) by the well-diffusion technique can be found in the Supporting Information. The antimicrobial activity of the PCDO and ECDO against *E. coli* and *S. aureus* by agar-well diffusion method was shown in the Fig. 7. Among these two strains, the negative strain *E. coli* showed better inhibitory effect towards the samples and the *S. aureus* remained as potent strain. The diameter of zone of inhibition against *E. coli* and *S. aureus* were measured as 4.2 ± 0.3 cm, 3.2 ± 0.2 cm, 3.7 ± 0.3 cm and 2.2 ± 0.2 cm, 1.5 ± 0.3 cm, 1.8 ± 0.2 cm, respectively for amoxicillin, PCDO and ECDO. Generally, the cell wall of the gram-positive bacteria is thicker due to the presence of peptidoglycan layer which is not present in the gram-negative bacteria. This layer prevents the penetration of metal ions into the cytoplasm [46]. The doping of Eu into cerium dioxide could possibly enhance the specific surface area of CeO_2 resulting in the excessive production of reactive oxygen species [47]. Thereby the inhibition on ECDO was increased when compared to the PCDO samples. Thus, the ECDO material can be used in the sewage treatment despite of its dye degradation properties.

4. Conclusions

In summary, PCDO and ECDO nanoparticles were produced in single phase and high purity using the facile glycine-assisted hydrothermal process. The results of the powder XRD showed the cubic fluorite structure for both the PCDO and ECDO samples. The crystallite size, d-spacing, lattice constant and volume of PCDO and ECDO samples were determined from the prominent scattering angles seen in the XRD pattern and the results were compared. The well dispersed spherical-like morphologies of the PCDO and ECDO samples with grain sizes of 13 and 10 nm were observed from the TEM analysis, which is comparable to the XRD results. The Eu element incorporated in the CeO_2 was proved by the EDX and XPS results. In the UV–visible and PL studies, a strong optical absorption band and a remarkable luminescence emission peak of the ECDO were observed compared to the PCDO sample. The ferromagnetic activity of the ECDO sample was detected in the VSM analysis and its magnetic parameters were also analyzed from the M−H loop results. In contrast to the PCDO sample, improved photodegradation performance and antibacterial activity of the ECDO have been identified and can be used for sewage treatment.

CRediT authorship contribution statement

S. Gnanam: Methodology, Investigation, Writing - review & editing. **J. Gajendiran:** Investigation, Writing - review & editing, Conceptualization. **J. Ramana Ramya:** Formal analysis. **K. Ramachandran:** Formal analysis. **S. Gokul Raj:** Formal analysis.
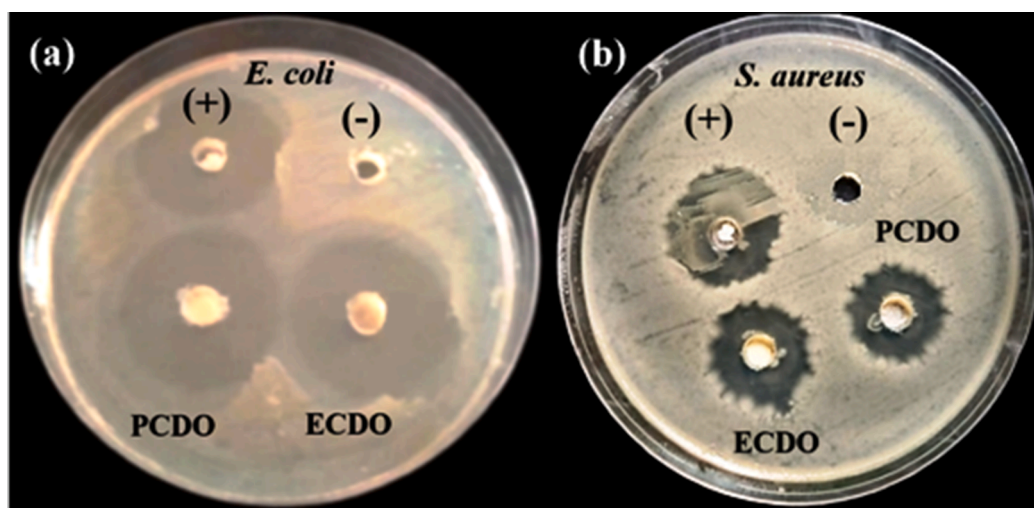
Fig. 7. Antibacterial activities of PCDO and ECDO samples against (a) the gram-negative strain *E. coli* and (b) the gram-positive strain *S. aureus*.

Declaration of Competing Interest

The authors declare that they have no known competing financial interests or personal relationships that could have appeared to influence the work reported in this paper.

Appendix A. Supplementary data

Supplementary data to this article can be found online at https://doi.org/10.1016/j.cplett.2020.138217.

References

[1] B. Bayyappagari, K. Shaik, M.R. Nasina, O. Inturu, R. Dugasani, Optik. 154 (2018) 821–827.
[2] A. Bouaine, R.J. Green, S. Colis, P. Bazylewski, G.S. Chang, A. Moewes, E. Z. Kurmaev, A. Dinia, J. Phys. Chem. C. 115 (5) (2011) 1556–1560.
[3] S. Soni, R.S. Sudish Kumar, V.S. Meena, S.D. Vats, AIP Conference Proceedings. 1665 (2015) 130029.
[4] Swati Soni, V. S. Vats, Sudhish Kumar, B. Dalela, Monu Mishra, R. S. Meena et al., J. Mater. Sci: Mater. Elect. 29 (2018) 10141-10153.
[5] R. Niruban Bharathi, S. Sankar, Superlattices and Microstructures. 123(2018) 37-51.
[6] R. Niruban Bharathi, S. Sankar, J.Supercond. Nov. Magn. 31(2018) 2603-2615.
[7] R. Niruban Bharathi, S. Sankar, J. Materi. Sci. Mater. Elect. 29 (2018) 6679–7669.
[8] X. Chen, G. Li, Y. Su, X. Qiu, L. Li, Z. Zou, Nanotechnology. 20 (2009) 115606.
[9] Vijay Singh, G. Sivaramaiah, J. L. Rao, N. Singh, Anoop K. Srivastava, Pramod K. Singh et al. J. Mater. Sci: Mater. Elect. 27 (2016) 4494-4500.
[10] L. Li, H.K. Yang, B.K. Moon, Z. Fu, C. Guo, J.H. Jeong, et al., J. Phys. Chem. C. 113 (2009) 610–617.
[11] S. Yang, Z. Jiang, Y. Zhang, J. Mater. Sci. Mater. Elect. 29 (2018) 7952–7956.
[12] Z.L. Wang, G.R. Li, Y.N. Ou, Z.P. Feng, D.L. Qu, Y.X. Tong, J. Phys. Chem. C. 115 (2011) 351–356.
[13] L. Bi, H.S. Kim, Gerald F. Dionne, Scott A. Speakman, D. Bono, C. A. Ross, J.Appl. Phy.103 (2008) 07D138.
[14] D. Fang, M. Zhang, Z. Luo, T. Cao, Q. Wang, Z. Zhou, et al., Opt. Mater. 38 (2014) 1–5.
[15] K.Y. Jung, J.C. Lee, D.S. Kim, B.K. Choi, W.J. Kang, J. Luminescence. 192 (2017) 1313–1321.
[16] S. Fujihara, M. Oikawa, J. Appl. Phys. 95 (2004) 8002.
[17] A. G. Santiago, N. F. Andrade Neto, E. Longo, C. A. Paskocimas, F. V. Motta, M. R. D. Bomio, J. Mater. Sci. Mater. Elect. 30(2019) 11508-11519.
[18] S. Yildirim, S. Alper Akalin, S. Oguzlar, M.Z. Ongun, C. Ozer, M. Erol, J. Mater. Sci. Mater. Elect. 30 (2019) 13749–13756.

[19] E. Swatsitang, S. Phokha, S. Hunpratub, S. Maensiri, Physica B: Condensed Matter. 485 (2016) 14–20.
[20] Mônica A. Rodrigues, Ariadne C. Catto, Elson Longo, Edson Nossol, Renata C.Lima, J. Rare Earths. 36 (2018) 1074-1083.
[21] S.K. Alla, R.K. Mandal, N.K. Prasad, RSC Advance. 6 (2016) 103491–103498.
[22] S.K. Alla, P. Kollu, R.K. Mandal, N.K. Prasad, Cerm. Int. 44 (2018) 7221–7227.
[23] Jalpa A. Vara, Pragnesh N. Dave, SN. Appl. Sci.1(2019) 432.
[24] S. Li, X. Lu, S. Shi, L. Chen, Z. Wang, Y. Zhao, Front. Chem. 8 (2020) 348.
[25] W. Huang, Y. J. Tan, D. Li, H. Du, X. Hu, G, Li et al. J. Luminescence. 206 (2019) 432-439.
[26] M. El-Hagary, E.R. Shaaban, S.H. Moustafa, G.M.A. Gad, Solid State Sciences. 91 (2019) 15–22.
[27] K. Kumari, R.N. Aljawfi, Y.S. Katharria, S. Dwivedi, K.H. Chae, R. Kumar, et al., J. Electron Spectroscopy and Related Phenomena. 235 (2019) 29–39.
[28] S. Shanmuga Sundari, S. Sugan, G. Pabitha, Mater. Today. Proc. 5 (2018) 6633–16639.
[29] C. Xia, C. Hu, P. Chen, B. Wan, X. He, Y. Tian, Mater. Res. Bull. 45 (2010) 794–798.
[30] L. Sun, Y. Tan, D. Li, H. Du, D. Guo, Opt. Mater. 100 (2020) 109654.
[31] S. Chaudhary, S. Kumar, S.K. Mehta, Mater. Sci. Eng: C. 96 (2019) 263–271.
[32] Z. Yang, Z. Yin, Z. Zhao, J. Yu, J. Li, Z. Ren, et al., Mater. Chem. Phy. 240 (2020) 122148.
[33] Z. Yang, Z. Zhao, J. Yu, J. Li, Z. Ren, S. Ma, et al., Ceram. Int. 45 (2019) (1933) 11927–11931.
[34] X. Ma, P. Lu, P. Wu, J. Alloys. Comp. 734 (2018) 22–28.
[35] F.A. Al-Agel, E. Al-Arfaj, A.A. Al-Ghamdi, Y. Losovyj, L.M. Bronstein, W. E. Mahmoud, J. Mag. Mag. 360 (2014) 73–79.
[36] M. A. Majeed Khan, Wasi Khan, M. Naziruddin Khan, Abdulaziz N. Alhazaa, J. Mater. Sci. Mater. Elect. 30 (2019) 8291-8300.
[37] S. Phokha, S. Pinitsoontorn, S. Maensiri, J. Appl. Phys. 112 (2012) 113904.
[38] P. Wang, F. Meng, C. Gao, W. Xie, J. Wang, A. Li, J. Mater. Sci. Mater. Elect. 29 (2019) 11482–11488.
[39] J. Malleshappa, H. Nagabhushana, S.C. Prashantha, S.C. Sharma, N. Dhananjaya, C. Shivakumara, B.M. Nagabhushana, J. Alloys. Comp. 612 (2014) 425–434.
[40] L. Qin, X. Niu, J. Mater. Sci. Mater. Elect. 27 (2016) 12233–12239.
[41] K. Anandan, K. Rajesh, K. Gayathri, V. Rajendran, Materials Today: Proceedings. (2020) Article in Press.
[42] J. Liqiang, Q. Yichun, W. Baiqi, L. Shudan, J. Baojiang, Y. Libin, et al., Solar Energy Materials & Solar Cells. 90 (2006) 1773–1787.
[43] Ivan G.N. Silva, Alysson F. Morais, Luís F.M. Zambon , Hermi F. Brito, Danilo Mustafa, Optic. Mater. 76 (2018) 48-55.
[44] W. Gao, J. Li, X. Zhou, Z. Zhang, Y. Ma, Y. Qu, J. Mater. Chem. C. 2 (2014) 8729–8735.
[45] Vasile I. Parvulescu, C. Tiseanu, Catalysis Today. 253 (2015) 33-39.
[46] L.K. Adams, D.Y. Lyon, P.J. Alvarez, Water Research. 40 (2006) 3527–3532.
[47] J. Liu, J. Ma, Y. Bao, J. Wang, Z. Zhu, H. Tang, et al., Composites Science and Technology. 98 (2014) 64–71.